
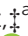




Cite this: *Sens. Diagn.*, 2024, **3**, 659

Integration of melt electrowritten microfibers with magnetoelastic sensors for continuous monitoring of cell growth†

William S. Skinner, ^{‡a} Paula G. Saiz, ^{‡ab} Ander Reizabal,^{ac} Jeffrey E. Plumley,^a Paul D. Dalton^a and Keat Ghee Ong ^{id *a}

Magnetoelastic sensors, which are wirelessly activated and interrogated via magnetic fields, have gained popularity for monitoring physical parameters such as mass loading and stress. The functionalization of the sensor surface has facilitated the development of biosensing devices with the capacity to monitor chemical/biological quantities such as liquid pH, bacteria, and cell growth in biological environments. In this study, melt electrowriting (MEW) is used for the first time to integrate user-defined microstructures onto the surface of magnetoelastic sensors, aiming to enhance their cell growth monitoring performance. Specifically, MEW is used to define specific topographies on the sensor surface, which enable custom control of attachment, distribution, and alignment of cells along the sensor surface. This technique holds potential for engineering tissues with predefined physical structures, as well as for the development of advanced monitoring systems for tracking the growth of adherent cells in real-time.

Received 1st February 2024,
Accepted 5th March 2024

DOI: 10.1039/d4sd00039k

rsc.li/sensors

1. Introduction

Magnetoelastic sensors have garnered attention in both the scientific community and manufacturing industry due to their ability to wirelessly monitor various types of physical, chemical and biological quantities such as mass,^{1,2} pressure,^{3,4} pH,^{4,5} chemical compounds,^{2,6–9} bacteria,^{10–16} cells,^{17–19} etc. The operation of those sensors is based on their magnetoelastic property, which causes them to vibrate at a specific resonance frequency when excited by a frequency-varying alternating magnetic field. As the sensor is exposed to different environmental conditions, such as changes in temperature, liquid viscosity, or mass loading on its surface, both the magnitude and frequency of its resonance undergo changes. Utilizing magnetic interrogation solenoids allows for the wireless measurement of the sensor's resonance variation, enabling the determination of alterations in the environmental conditions surrounding the sensor. For

chemical and biological sensing, the sensor's surface can be modified with coatings that selectively interact with the target analyte, transforming the presence of the analyte into a physical change, such as mass. Functional coatings have been applied to magnetoelastic sensors, facilitating the monitoring of various physical, chemical, and biological parameters and processes. Examples include humidity monitoring with titanium dioxide nanotubes,^{20–24} toluene detection with metal-organic chemical frameworks,² heavy metal sensing with graphene oxide,⁷ and even viral and bacterial detection with bioreceptors.^{7,10–16,25,26} Recent studies have suggested the possibility of enhancing the sensor's sensitivity by adjusting the degree of modification in different regions of the sensor.^{27,28} Given that the sensitivity of the sensor is not uniform across its surface, controlled load attachment throughout the sensor surface could enhance the robustness and reliability of the sensing platform. This is particularly important for certain applications such as adherent cell monitoring, where cells can attach to the surface in a non-uniform distribution.

The wireless nature of magnetoelastic sensors make them excellent candidates for use in controlled biological environments such as viral, bacterial, or cellular cultures.^{29,30} Previous work has demonstrated the use of these sensors to monitor adherent cell growth and modulate cell adhesion.^{18,19,31–34} However, these studies have noted a non-uniform distribution of cells across the sensor and reduction in cell attachment associated with the sensor activity. Consequently, there is a need to develop surface modification

^a Phil and Penny Knight Campus for Accelerating Scientific Impact, University of Oregon, 1505 Franklin Boulevard, Eugene 97403, OR, USA.

E-mail: kgong@uoregon.edu
^b Macromolecular Chemistry Research Group (LABQUIMAC), Dept. of Physical Chemistry, Faculty of Science and Technology, University of the Basque Country (UPV/EHU), 48940 Leioa, Spain

^c BCMaterials, Basque Center for Materials, Applications and Nanostructures, Bldg. Martina Casiano, UPV/EHU Science Park, Barrio Sarriena s/n, 48940 Leioa, Spain

† Electronic supplementary information (ESI) available. See DOI: <https://doi.org/10.1039/d4sd00039k>

‡ These authors have contributed equally to the work.



to control cell adhesion across the sensor surface.^{31,34,35} Some common methods for integrating homogeneous coatings onto the surface of magnetoelastic sensors include spin coating, dip coating, and vapor deposition. Additionally, electrospinning has recently been explored for increasing the active surface area of magnetoelastic sensors and thereby improving their overall response.^{9,24} Electrospun coatings are highly functionalizable, making them especially promising in this application.^{36,37} Despite the variety and versatility of these techniques, previous studies have focused on functionalization of the entire sensor surface and lack the capability to introduce user-defined microstructures onto the magnetoelastic sensor surface. Controlled surface functionalization at the local level could improve sensor performance by defining specific surface roughness or promoting higher mass gain in the most sensitive regions of the sensor.

In this context, this work explores the application and effect of melt electrowriting (MEW)³⁸ to define different tailored microstructures onto the magnetoelastic sensor surface, aiming to tune its overall response. MEW is a high-resolution 3D-printing technique that leverages electrohydrodynamic phenomena to yield exceptional control over microfiber deposition.^{39,40} Furthermore, MEW has the capacity to process various materials, including functionalizable polymers and material composites, making it a versatile technique.⁴¹ While MEW has been primarily used for fabricating scaffolds with custom microstructures and mechanical properties that mimic the extracellular matrix,^{42–44} this work focuses on integrating defined MEW structures onto the magnetoelastic sensor surface to enhance the sensor's performance in monitoring cell growth. Cells have been previously reported to attach and grow with a non-uniform density across magnetoelastic sensor surfaces.¹⁹ Therefore, precise control over cell attachment density at different regions of sensitivity on the sensor surface could result in a more reliable and robust monitoring system. Additionally, previous work has shown that high magnitudes of vibration of magnetoelastic sensors can cause adherent cells to detach from their sensor surface.³¹ Thus, the feasibility of MEW coatings to mitigate some of this detachment by increasing the available surface area⁴⁵ for cells to adhere to will be further investigated.

This work describes a feasible method for integrating various MEW microstructures onto the surface of magnetoelastic sensors. The stability of these microstructures under different conditions is evaluated, demonstrating the good adherence of the deposited layers. Subsequently, the sensor performance is characterized by examining its response when loaded with growing human mesenchymal stromal cells (hMSCs). Specifically, the effect of the MEW microstructures on the attachment and distribution of hMSCs on both resonating and non-resonating modes is investigated. The capability to define MEW microstructures as the active surface of magnetoelastic sensors results in a highly tunable and versatile sensing platform that allows for tuning cell density across the sensor surface, holding potential for various applications.

2. Experimental

2.1 Materials

Metglas® 2826MB amorphous ferromagnetic alloy employed as the sensor material was obtained commercially in the form of a rolled ribbon of 29 µm thick and 12.7 mm wide (Metglas® Inc., Conway SC, USA). Metglas® 2826MB was used for its exceptional magnetic and magnetoelastic properties (saturation magnetization = 0.39 T, coercive force <50 A m⁻¹), low cost, and high corrosion resistance.⁴⁶ Medical grade poly(ε-caprolactone) (PCL) (PURASORB® PC 12, 2007001461, Corbion, Amsterdam, Netherlands) was used to create the MEW scaffolds. Granular dichloro-*p*-cyclophane (DPX-C, Specialty Coating Systems Inc., Indianapolis, IN, USA) was used in combination with a PDS 2010 Labcoter® (Specialty Coating Systems Inc., Indianapolis, IN, USA) to deposit a conformal layer of parylene-C onto the surface of sensors with and without MEW microstructures. Finally, xeno-free media (RoosterBasal-MS-CC, RoosterBio, Frederick, MD, USA), penicillin-streptomycin (Sigma-Aldrich, St. Louis, MO, USA), xeno-free supplement (RoosterBooster-MS-CC, RoosterBio, Frederick, MD, USA), 0.25% trypsin-EDTA (Gibco, Invitrogen, Waltham, MA, USA), phosphate-buffered saline (PBS) (endotoxin-free Dulbecco's PBS 1× w/o Ca⁺⁺ & Mg⁺⁺, MilliporeSigma, Burlington, MA, USA), 32% paraformaldehyde (PFA) aqueous solution (Electron Microscopy Sciences, Hatfield, PA, USA) and Hoechst nuclei stain solution (Hoechst 33342, trihydrochloride, trihydrate, ThermoFisher, Waltham, MA, USA) were obtained from their respective suppliers and used as recommended for the culturing and quantification of cells.

2.2 Sensor fabrication

Free-standing rectangular sensors of 5 mm × 12.7 mm were cut from the Metglas® 2826MB ribbon roll by using a high-power pulse laser (Coherent ExactCut 430, Coherent, Santa Clara, CA, USA) and subsequently cleaned with ethanol and annealed in an oven (Model 10 Lab Oven, Quincy Lab, Inc., Burr Ridge, IL, USA) at 125 °C for 2 hours. Following the annealing of the sensors, they were characterized by measuring the real part of the S11 parameter using a network analyzer (Keysight ENA E50618, Keysight Technologies, Santa Rosa, CA, USA) with a custom-wound interrogation solenoid (see section 2.5 for details). Sensors were then sorted into groups, so that the response magnitudes of sensors in each group were within 5% of their expected full-scale output, defined as the difference in response magnitude between the start of the cell experiment and after the final sensor signal was recorded. Afterward, PCL scaffolds were printed directly onto a set of sensors using MEW. To accomplish this, a magnet was placed on the printing collector beneath a glass slide to keep the sensors in place during the printing process. Sensors were placed on the glass slide and MEW fibers were deposited onto the sensor surface, past the edges of the sensor (see section 2.3 for details of the MEW process). The excess scaffold material over the edges of the sensor was trimmed with a VLS 2.30 laser cutting machine (Universal Laser Systems, USA), which also improved the



adhesion of the scaffold fibers to the sensor by partially melting the scaffold around the edges of the sensor. Next, these sensors were coated with a 10 μm -thick conformal parylene-C layer (PDS 2010 Labcoter system, SCS, USA) to improve corrosion resistance and facilitate biocompatibility.¹⁸ Afterwards, sensors were treated with oxygen plasma in a reactive ion etching system (March Jupiter II RIE, USA) for 30 s at 100 W to promote cell adhesion. Finally, fabricated sensors were cleaned with 70% ethanol, allowed to dry, placed in sterilization pouches, and sterilized with ethylene oxide gas before using them in cell culture experiments. Fig. 1 illustrates the sensor preparation and cell growth detection process. In addition to these sensors, a set of sensors without MEW scaffolds were also prepared using the same protocol (except the MEW printing step) to serve as controls for the experiment.

2.3 Melt electrowriting process

PCL microstructures were electrowritten onto the surface of magnetoelastic sensors using a custom-built MEW device.⁴⁷ Briefly, the device consists of a moving collector that is controlled by two linear stages (X/Y) and a heated print head containing a 27-G nozzle plastic syringe (Nordson EFD) connected to an air pressure controller (SMC, USA). A high-voltage source is used to create an electrical potential difference between the positively charged nozzle and the grounded collector. For the electrowriting process, the distance between the collector and the nozzle was set to 3 mm while the voltage, temperature, and pressure were set to 4 kV, 85 $^{\circ}\text{C}$, and 260 kPa, respectively. The jet speed at these conditions, determined by measuring the critical translation speed, was 350 mm min^{-1} .⁴⁸ This allowed PCL microstructures to be fabricated at a speed of 480 mm min^{-1} from 10 μm thick fibers without excessive jet stretching.

2.4 hMSCs culture

Human bone marrow-derived mesenchymal stem cells (hMSCs) were used for cell culture experiments. Cells were commercially obtained (donor #000175, female, 28 years old,

RoosterBio, Frederick, MD, USA), expanded according to manufacturer's protocol, and cryogenically stored in liquid nitrogen. Prior to use, cells were recovered from liquid nitrogen, thawed, seeded at 5000 cells per cm^2 , and cultured until confluent. These cells were cultured in xeno-free media and supplemented with 1% penicillin-streptomycin and xeno-free supplement. Once confluent (~ 72 hours, confirmed *via* light microscopy), cells were lifted with 0.25% trypsin-EDTA, counted using an automatic cell counter (NucleoCounter NC-200, Chemometec, USA), and then resuspended in media to the target seeding density. Cells were incubated at 37.0 $^{\circ}\text{C}$, 93% relative humidity, and under 5% CO_2 in a microbiological incubator (HERAcell VIOS 160i, Thermo Fisher Scientific, USA).

Each sensor was placed inside a 2-well chamber slide (Nunc Lab-Tek II Chamber Slide system, Thermo Fisher Scientific) on top of a 3D-printed grated stage. The stage, 3D-printed with an autoclavable and biocompatible resin (High Temp v2, FormLabs, Somerville, MA, USA), has a recessed retainment area designed to allow the sensor to vibrate freely while remaining at the same position. All stages were cleaned with 70% ethanol in an ultrasonic cleaner (CO-Z supplies, Lake Forest, USA) for 5 minutes, placed inside sterilization pouches, and then autoclaved (Beta Star Small Sterilizer Autoclave, Beta Star, Honey Brook, USA). After placing the sterilized sensors on the grated stage in the 2-well chamber slide (see Fig. 1), cells were seeded at varying densities ranging from 10 000 cells per cm^2 to 40 000 cells per cm^2 . Culture volume was seeded at 2 ml to ensure the sensor and cells remained submerged for a period of at least 6 days. Finally, the chamber slide was placed inside the interrogation solenoid to wirelessly activate and capture the resonance spectrum of the sensor in real time.

2.5 Sensor characterization

The sensor signals were remotely captured using an experimental set-up that was modified from our previous work.¹⁹ The detection system included a neodymium magnet

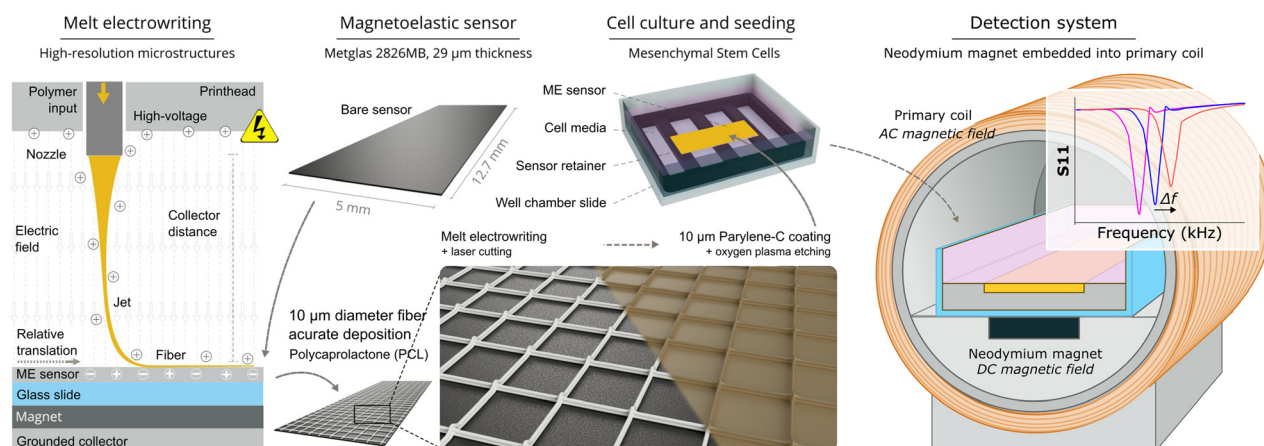


Fig. 1 Schematic diagram highlighting key details of sensor preparation and the magnetoelastic monitoring system.



(B4201, K&J Magnetics, Pipersville, PA, USA) to maximize the magnetostriction of the sensor and increase its resonance amplitude. The magnet was embedded inside an interrogation solenoid (24 AWG, 135 turns, 2 layers, 39 mm in diameter, 39 mm in length) which applied an AC magnetic field that caused the sensor to resonate, while also captured the sensor signal by measuring the S11 parameter of the solenoid. The S11 parameter of the interrogation solenoid was measured with a tabletop network analyzer (Keysight ENA E50618, Keysight Technologies, Santa Rosa, CA, USA) or a portable network analyzer (NanoVNA-F, Hangzhou Minghong Electronic Technology Co., Ltd., Hangzhou, China). The network analyzer and the transmission cables for connecting the interrogation solenoids were calibrated together with a manual open-short-load calibration kit (Hangzhou Minghong Electronic Technology Co., Ltd., Hangzhou, China). The network analyzer captured and saved the resonance spectrum of the sensor into data files, which were later analyzed and plotted on a computer. A background measurement, generated by collecting the resonance spectrum of the solenoid without a sensor, is subtracted from all sensor measurements to eliminate the effect of the solenoid's impedance on the sensor resonance measurement. To monitor the attachment and growth of cells, sensors seeded with cells were positioned in the interrogation solenoid such that the maximum possible signal was observed on the network analyzer display. The baseline resonance spectrum for each sensor was measured immediately after the addition of cell suspension, marked as the first measurement (0 h). Subsequent resonance spectra were captured every 15 minutes following the 0 h measurement, creating a profile of cell growth over 6 days.

Immediately after collecting the endpoint resonance spectrum, quantification of cell nuclei was conducted to investigate the relationship between changes in the sensor signal and the attachment, growth, and distribution of cells on the sensor surface. The process involved aspirating culture media from the well containing the sensor, rinsing the well with PBS, and aspirating the rinse. Subsequently, cells were fixed by incubating the sensors for 10 minutes in a solution of 4% PFA diluted in PBS. After aspirating the PFA solution, the nuclei of the cells were stained by incubating them for 10 minutes in a solution of Hoechst 33342 nuclei stain, diluted to $50 \mu\text{g mL}^{-1}$ in PBS. Following this incubation period, the staining solution was aspirated, and the sensor was carefully inverted into the empty, unused well of the chamber slide. The sensor was covered with PBS, and the chamber slide was wrapped in aluminum foil to protect it from exposure to ambient light. Fluorescent microscopic imaging was performed using a confocal fluorescence microscope (CSU-W1 SoRa, Nikon, Japan) with a DAPI (4',6-diamidino-2-phenylindole) filter to show the stained nuclei. To quantify the number of cells attached to the sensor surface, representative images of $1 \text{ mm} \times 1 \text{ mm}$ were taken for each sensor in 12 specific locations that were kept consistent for each sensor. Cell nuclei were quantified through the analysis

of fluorescence microscope images using custom MATLAB analysis software.

Finite element analysis (FEM) simulations of the first resonance frequency mode of the sensors were performed using COMSOL Multiphysics® software (COMSOL AB, Stockholm, Sweden) to determine local extremes in sensitivity along the sensor surface and hence define a microstructure according to those results. The microstructure and morphology of the PCL scaffold layers were visualized with a digital microscope (VHX-7000, Keyence, USA), as well as by a scanning electron microscope (SEM) (Apreo 2, Thermo Fisher, USA) to characterize the scaffold geometry and confirm adhesion and stability of the microstructure defined above the sensor surface.

3. Results

3.1 MEW printability on the sensor surface and effect on the sensor signal

First, the quality of the printing onto the magnetoelastic sensor surface was optically investigated, showing that it was comparable to that achieved when printing directly onto the collector.⁴⁹ Under the conditions described previously, fibers of around $9.6 \pm 0.2 \mu\text{m}$ in diameter with a minimum interspace of around $90 \mu\text{m}$ onto different microstructures were achieved (Fig. 2A). The placement of a magnet beneath the glass slide to hold the magnetoelastic sensors during the printing process was essential, as movement of the collector during printing could otherwise displace the sensors and disrupt fiber deposition. The MEW microstructures were printed beyond the sensor edges, with the excess material later trimmed off with laser. This process further melted the fibers near the sensor edges (Fig. 2B), causing them to adhere better onto the sensor surface.

Various microstructures were designed and printed onto the sensor surface to investigate its performance. Specifically, square microstructures with a fixed interspace of $500 \mu\text{m}$ and a varied number of layers (1, 2, 5 and 10) were printed onto the magnetoelastic sensors to determine the effect of these coatings on the resonance frequencies and magnitudes. The results indicate that the sensor magnitude decreased as the number of deposited layers increased due to the increased mass loading from additional MEW fibers (Fig. 2C). Despite the dampening of the sensor resonance by the microstructures, the *Q* factor of the resonance profile was only decreased by 25% for 10 layers of microstructure and 8% for 2 layers, supporting the use of MEW microstructures on magnetoelastic sensors.

In addition, a microstructure with a gradual pore size going from very small rectangular pores of $100 \times 500 \mu\text{m}$ on the sensor tips to bigger pores that increase progressively was designed following the tendency of the sensitivity along the longitudinal length of the sensor simulated in COMSOL (Fig. 2D). This demonstrates the versatility of MEW technique to define specific microstructures above magnetoelastic sensors, including the possibility to deposit different



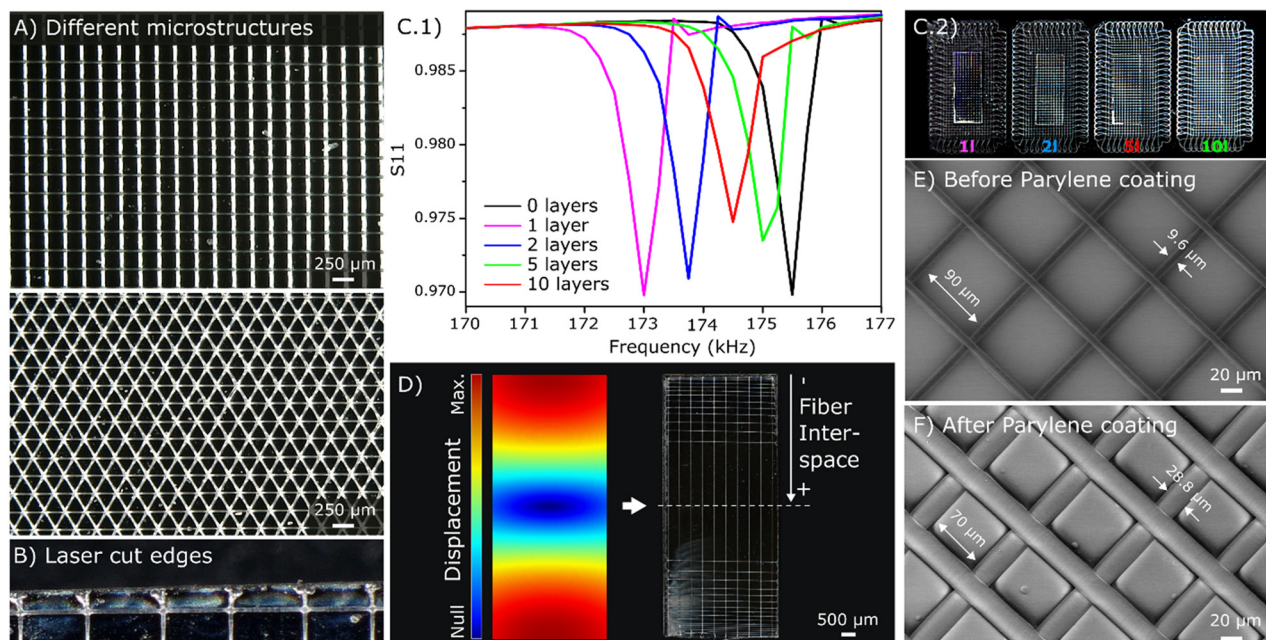


Fig. 2 A) Different PCL microstructures directly printed onto the magnetoelastic sensor surface. B) Detail of the laser cut edge following PCL deposition, where the fibers at the sensor's edges melted, enhancing scaffold adhesion to the sensor, C) magnetoelastic resonance measurements (C.1) showcasing the impact of increasing number of layers in the MEW microstructure deposited on the sensor (C.2), D) COMSOL simulation of the resonance displacement and sensitivity across the sensor surface and gradual MEW microstructure designed following the sensitivity profile along the longitudinal direction, E and F) SEM images of the MEW microstructure before and after the parylene-C coating.

amounts of material in zones⁵⁰ with different sensitivities for a more effective sensing process, which can find applications in different areas.

3.2 Evaluation of the MEW coating

After deposition MEW fibers onto the magnetoelastic sensors, the stability of these microstructures was assessed using SEM after exposure to air and liquid media. The same evaluation was repeated following parylene-C coating and plasma etching of the sensors. This assessment was conducted for samples with different numbers of layers and fiber sizes, and the results indicated that the microstructure morphology and adhesion were maintained after parylene-C coating and plasma etching. SEM images revealed that the median diameter of the microfibers increased from $9.6 \pm 0.2 \mu\text{m}$ for the bare PCL fibers (Fig. 2E) to around $28.8 \pm 0.4 \mu\text{m}$ after the parylene-C coating (Fig. 2F). This resulted in a decrease in the median pore size from around $90 \times 90 \mu\text{m}$ to $70 \times 70 \mu\text{m}$, confirming the $10 \mu\text{m}$ thickness of the parylene-C coating. A similar morphology was observed after the plasma etching, affirming that this process did not affect the defined microstructure.

Sensors coated with MEW microstructures were also placed in water and activated with an interrogation solenoid to investigate the stability of the MEW layer in liquid media. No detachment of the microstructure from the sensor surface was observed, indicating the microstructures were physically stable even through the sensor vibration and in liquid media.

Similar experiments were conducted for sensors with the parylene-C coating and plasma etching, and no differences were observed in terms of stability.

3.3 *In situ* monitoring of cell growth

While magnetoelastic sensors have been utilized as a sensing platform for non-invasive real-time monitoring of cell growth, certain challenges have been identified with this approach. Notably, resonance activity of the sensors at relatively high magnitudes has been linked to the detachment of cells,^{31,34} potentially compromising the accuracy of measurements. Additionally, in the early stages of cell growth and attachment (<24 hours), a non-uniform distribution of cell density along the sensor surface was observed which could affect the reliability of measurements due to the variance of sensitivity across the sensor surface.^{28,51} In addressing these challenges, the incorporation of a MEW microstructure on the sensor surface holds promises as it can increase the available surface area and introduce 3D structures for cells to attach to, potentially alleviating these issues.

MEW has been commonly employed to develop scaffolds for 3D cell culture.⁴¹ Several studies have highlighted the significance of the scaffold geometry, including pore size, shape, fiber diameter, and stiffness, as a key factor that can influence cellular behavior.^{52,53} In particular, a recent study investigating osteogenesis in hMSCs demonstrated the benefits of using $100 \mu\text{m}$ square PCL scaffolds fabricated *via* MEW. Compared to other pore sizes, $100 \mu\text{m}$ square scaffolds



facilitated a higher seeding efficiency while maintaining a spread cellular morphology.⁵⁴ Based on these results, a microstructure with 100 μm size square pores was selected to investigate the effects of the microstructure on cell adherence and growth at the sensor surface. MEW microstructures with 100 μm square pores and a varied number of layers (1, 2 and 5) were printed onto magnetoelastic sensors and investigated in terms of magnetoelastic signal and cell attachment and distribution. First, magnetoelastic measurements indicated that the 5-layer microstructures severely dampened the sensor signal, leading to its exclusion from further investigation. In contrast, the 2-layer microstructures reduced the Q factor by only 8% compared to the uncoated sensor. The dampening of the signal reduced the sensors' sensitivity to cell loading. In the selection of the coatings for further investigation, it was important to consider the balance between the control over cell adhesion and the preservation of sensor signal magnitude and quality. Therefore, the 1-and 2-layer sensors were further investigated in terms of cell growth. Sensors with and without the MEW microstructures were seeded with human mesenchymal stromal cells (hMSCs) at a density of 40 000 cells per cm^2 and incubated for 24 hours to investigate the cells' attachment and distribution across the sensors. Results indicated that the average cell density was slightly higher on the sensors without microstructures. However, the sensors with microstructures showed improvement in the uniformity of cell density as the number of layers increased, as shown in Fig. 3. Observation of the MEW structure on the fluorescent images demonstrated the stability of the defined microstructure even

after prolonged exposure to cell media, which is an important consideration in the application of the sensors with MEW microstructures for monitoring cell growth and other parameters in liquid media.

Microstructures with a gradual pore design (Fig. 2D) were employed to further investigate the possibilities of MEW microstructural design in tuning cell distribution along the sensor surface. The density of cells along this geometry was explored, revealing that this design allowed for further tuning of cell density across the sensor, increasing the variance in cell density across the sensor surface. Specifically, fluorescence microscopy showed that for these gradual pore size scaffolds, there were fewer cells attached in the regions with smaller pore sizes. This highlights a key advantage of using MEW fibers on top of magnetoelastic sensors since the pore size along the structure could be precisely tuned to partially avoid cell attachment or implement other functionalities on specific regions of the sensor.

After confirming cell attachment and proliferation on the sensors with the MEW microstructures, cell growth was continuously tracked over a 6 day period by measuring the resonance profile of the sensors. For this purpose, the 2-layer sensors with a 100 μm pore size were selected, along with the bare sensors for reference. The prepared sensors were placed in a chamber slide, seeded with cells at a density of 12 000 cells per cm^2 and the resonance spectrum was captured immediately and then once every 15 minutes for 6 days to generate growth profiles of hMSCs with and without the MEW microstructures. The change in the real portion of the S11 scattering parameter, a measurement directly related to

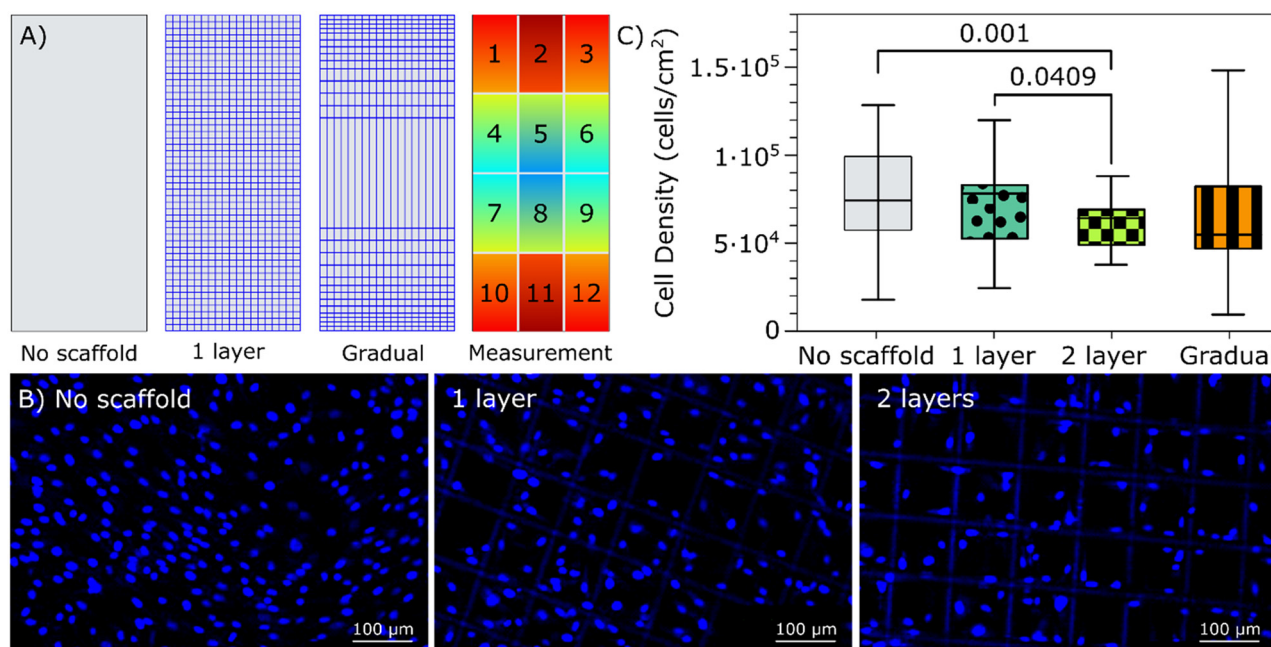


Fig. 3 A) Scheme of the different sensors investigated for cells attachment and of the different key zones analyzed, B) images and C) quantification for cells attachment on the sensors with and without MEW microstructures 24 hours after seeding. Cells were counted from fluorescence microscope images taken in key areas of the sensor ($n = 48$) and the average cell density per unit area was calculated. The error bars are indicative of the variance in cell density across the sensor surface. One-way ANOVA with Tukey's multiple comparisons test.



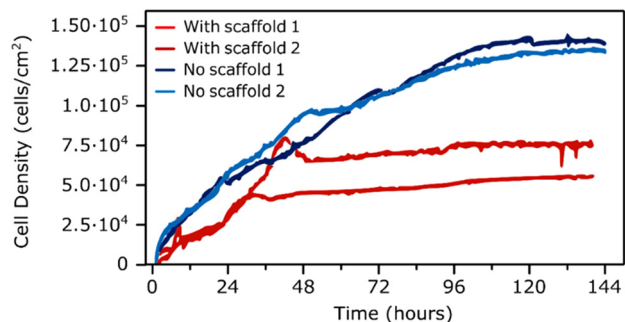


Fig. 4 Cell growth profiles resulted from plotting the measured change in S11 parameter at the resonance frequency normalized to the final cell density against the elapsed time.

the magnitude of the sensor resonance, was recorded as a function of time (Fig. 4). This indicates the capacity of those sensors for continuous and wireless monitoring of cell growth during culture. The overall change in signal magnitude was normalized to the average cell density quantified on the sensor surface and plotted against the elapsed time. Comparison of the generated growth profiles suggests that the presence of MEW microstructure may inhibit the growth and proliferation of hMSCs compared to sensors without the microstructure. Cell growth plateaus after nearly two days for sensors with the MEW structure, while it continues until around day 5 for sensors without it.

In conclusion, cell adhesion under sensor resonance was investigated to determine if the MEW microstructures could improve the attachment or retention of the cells during resonance. Similar to previous experiments, the presence of the MEW microstructures improved the uniformity in cell density across the active sensor surface compared to sensor without the MEW layer. However, the reduction in average

cell density under resonance for the sensors with the MEW microstructure was similar to that measured for the sensors without the MEW microstructure, which indicates that the MEW microstructure does not improve the retention of cells under resonance (Fig. 5).

This study demonstrated that cell adhesion and proliferation on the surface of magnetoelastic sensors can be controlled by the incorporation of MEW microstructures on the sensor surface. Furthermore, specific microstructural designs, such as the gradual pore one shown here, can further facilitate the control of cell density at local regions along the sensor surface, taking advantage of regions with differences in sensitivity. Overall, the capacity to define complex microstructures on the surface of magnetoelastic sensors opens up numerous possibilities for different applications beyond monitoring cell growth.

4. Conclusions

The feasibility of using MEW to define different microstructures on magnetoelastic sensors has been demonstrated. Direct writing through MEW, followed by laser cutting, was found to be a good approach for integrating various MEW microstructures onto magnetoelastic sensors. This method resulted in good adhesion to the sensor surface, precise control over the microstructure, and excellent repeatability. Furthermore, the stability of the MEW microstructure in liquid media, as well as after parylene-C coating and plasma etching has been confirmed. Magnetoelastic resonance magnitude and quality were found to vary with the microstructure properties, including the number of layers, the pore size, and the scaffold geometry.

An evaluation of the performance of sensors with and without MEW microstructures as platforms for non-invasive and continuous monitoring of cell growth was conducted. This included an analysis of the change in resonance amplitude with cell density and time, as well as an analysis of the cells' distribution and attachment across the surface of sensors with and without the MEW microstructures. Results demonstrated that sensors with MEW microstructures can be used for monitoring cell growth while maintaining sufficient signal quality. The incorporation of MEW microstructures on the sensor surface can improve the uniformity of cell density across its surface. Analysis of the normalized growth profiles measured by monitoring the magnetoelastic resonance frequency suggests that the presence of the microstructure on the sensor inhibited the growth and proliferation of cells across its surface relative to sensors without the microstructure. Future work could explore additional functionalization of the microstructure sensor surface by altering the geometrical parameters and using additional cell-affinity coatings such as heparin and collagen to improve the attachment and uniformity of cells on the sensors. Overall, the incorporation of melt-electrowritten microstructures as a coating on magnetoelastic sensors resulted in a versatile sensing platform with highly tunable surface characteristics that can be

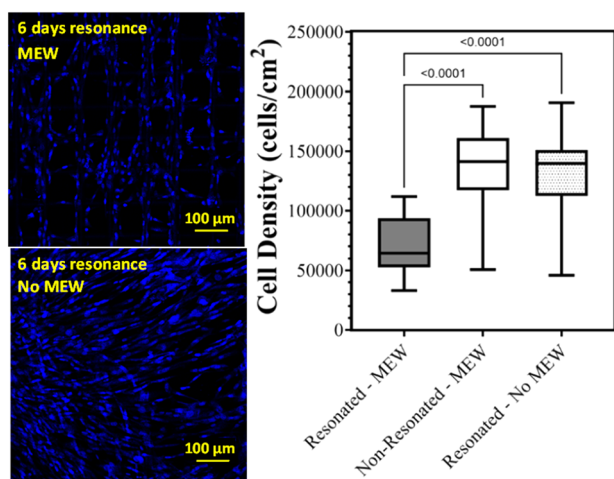


Fig. 5 Differences in attachment and retention of cells on the different sensors in the presence and absence of sensor resonance. Each group consists of 3 sensors, with 12 specific locations imaged for each sensor ($n = 36$). The error bars are indicative of the variance in cell density across the sensor surface. Two-way ANOVA with Tukey's multiple comparisons test was performed.



employed in a broad range of sensing applications in addition to monitoring cell growth.

Author contributions

Conceptualization, W. S. S., P. G. S., P. D. D. and K. G. O.; methodology, W. S. S. and P. G. S.; validation, W. S. S., P. G. S., and J. E. P.; formal analysis, W. S. S. and P. G. S.; investigation, W. S. S., P. G. S., and J. E. P.; resources, K. G. O. and P. D. D.; data curation, W. S. S., P. G. S., and J. E. P.; writing – original draft preparation, W. S. S. and P. G. S.; writing – review and editing, W. S. S., P. G. S., K. G. O., and P. D. D.; visualization, W. S. S., P. G. S., and A. R.; supervision, W. S. S., K. G. O., and P. D. D.; project administration, W. S. S., P. G. S., K. G. O., and P. D. D.; funding acquisition, K. G. O. and P. D. D.; all authors have read and agreed to the published version of the manuscript.

Conflicts of interest

There are no conflicts to declare.

Acknowledgements

This research was partially supported by the USA National Science Foundation, grant number EEC-1648035, and the Joe and Clara Tsai Foundation and the Wu Tsai Human Performance Alliance at Oregon, Phil and Penny Knight Campus for Accelerating Scientific Impact (Eugene, OR, USA). The support of the University of the Basque Country (UPV/EHU) for the Margarita Salas postdoctoral grant for P. G. S. under the “Convocatoria de ayudas para la recualificación del sistema universitario español para 2021–2023” is gratefully acknowledged. P. D. D. is supported by the Bradshaw and Holzapfel Research Professor in Transformational Science and Mathematics Fund.

Notes and references

- W. S. Skinner, S. Zhang, R. E. Guldborg and K. G. Ong, *Sensors*, 2022, **22**, 827.
- P. G. Saiz, R. Fernández de Luis, L. Bartolome, J. Gutiérrez, M. I. Arriortua and A. C. Lopes, *J. Mater. Chem. C*, 2020, **8**, 13743–13753.
- C. A. Grimes, P. G. Stoyanov, D. Kouzoudis and K. G. Ong, *Rev. Sci. Instrum.*, 1999, **70**, 4711–4714.
- M. K. Jain, Q. Cai and C. A. Grimes, *Smart Mater. Struct.*, 2001, **10**, 347.
- Q. Cai and C. A. Grimes, *Sens. Actuators, B*, 2000, **71**, 112–117.
- M. Zourob, K. G. Ong, K. Zeng, F. Mouffouk and C. A. Grimes, *Analyst*, 2007, **132**, 338.
- Y.-Q. Huang, J.-C. Yin, Y.-S. Wang, X.-L. Xiao, B. Zhou, J.-H. Xue, X. Tang, X.-F. Wang, Y.-F. Zhu and S.-H. Chen, *Sens. Actuators, B*, 2016, **235**, 507–514.
- A. Sagasti, J. Gutierrez, M. San Sebastian and J. M. Barandiaran, *IEEE Trans. Magn.*, 2017, **53**, 1–4.
- S. Atalay, B. Ates, S. Balcioglu, O. O. Inan, S. Kolak, M. Simsek, V. S. Kolat, S. Koytepe and T. Izgi, *IEEE Trans. Magn.*, 2021, **58**, 1–5.
- C. Ruan, K. Zeng, O. K. Varghese and C. A. Grimes, *Biosens. Bioelectron.*, 2004, **20**, 585–591.
- S. Huang, H. Yang, R. S. Lakshmanan, M. L. Johnson, J. Wan, I.-H. Chen, H. C. Wickle, V. A. Petrenko, J. M. Barbaree and B. A. Chin, *Biosens. Bioelectron.*, 2009, **24**, 1730–1736.
- R. Guntupalli, R. S. Lakshmanan, J. Hu, T. S. Huang, J. M. Barbaree, V. Vodyanoy and B. A. Chin, *J. Microbiol. Methods*, 2007, **70**, 112–118.
- R. S. Lakshmanan, R. Guntupalli, J. Hu, D.-J. Kim, V. A. Petrenko, J. M. Barbaree and B. A. Chin, *J. Microbiol. Methods*, 2007, **71**, 55–60.
- R. Guntupalli, J. Hu, R. S. Lakshmanan, T. S. Huang, J. M. Barbaree and B. A. Chin, *Biosens. Bioelectron.*, 2007, **22**, 1474–1479.
- C. Ruan, K. Zeng, O. K. Varghese and C. A. Grimes, *Anal. Chem.*, 2003, **75**, 6494–6498.
- P. Pang, S. Huang, Q. Cai, S. Yao, K. Zeng and C. A. Grimes, *Biosens. Bioelectron.*, 2007, **23**, 295–299.
- P. G. Saiz, R. Fernández de Luis, A. Lasheras, M. I. Arriortua and A. C. Lopes, *ACS Sens.*, 2022, **7**, 1248–1268.
- S. Shekhar, S. S. Karipott, R. E. Guldborg and K. G. Ong, *Biotechnol. Bioeng.*, 2021, **118**, 2380–2385.
- W. S. Skinner, S. Zhang, J. R. Garcia, R. E. Guldborg and K. G. Ong, *Sensors*, 2023, **23**, 1832.
- S. Atalay, T. Izgi, V. S. Kolat, S. Erdemoglu and O. O. Inan, *Sensors*, 2020, **20**, 425.
- C. A. Grimes and D. Kouzoudis, *Sens. Actuators, A*, 2000, **84**, 205–212.
- C. A. Grimes, D. Kouzoudis, E. C. Dickey, D. Qian, M. A. Anderson, R. Shahidain, M. Lindsey and L. Green, *J. Appl. Phys.*, 2000, **87**, 5341–5343.
- M. K. Jain, S. Schmidt, K. G. Ong, C. Mungle and C. A. Grimes, *Smart Mater. Struct.*, 2000, **9**, 502–510.
- A. Pena, J. D. Aguilera, D. Matatagui, P. de la Presa, C. Horrillo, A. Hernando and P. Marin, *Biosensors*, 2022, **12**, 1–17.
- K. G. Ong, K. Zeng, X. Yang, K. Shankar, C. Ruan and C. A. Grimes, *IEEE Sens. J.*, 2006, **6**, 514–523.
- A. L. Possan, C. Menti, M. Beltrami, A. D. Santos, M. Roesch-Ely and F. P. Missell, *Mater. Sci. Eng., C*, 2016, **58**, 541–547.
- P. G. Saiz, D. Gandia, A. Lasheras, A. Sagasti, I. Quintana, M. L. Fdez-Gubieda, J. Gutiérrez, M. I. Arriortua and A. C. Lopes, *Sens. Actuators, B*, 2019, **296**, 126612.
- A. DeRouin and K. G. Ong, *Smart Mater. Struct.*, 2016, **25**, 1–8.
- L. Ren, K. Yu and Y. Tan, *Materials*, 2019, **12**, 1135.
- K. M. Meyers and K. G. Ong, *Sustainability*, 2021, **13**, 13655.
- S. Trierweiler, H. Holmes, B. Pereles, R. Rajachar and K. G. Ong, *J. Biomed. Sci. Eng.*, 2013, **6**, 478–482.
- E. Vlaisavljevich, L. P. Janka, K. G. Ong and R. M. Rajachar, *IEEE Trans. Biomed. Eng.*, 2011, **58**, 698–704.
- H. R. Holmes, E. L. Tan, K. G. Ong and R. M. Rajachar, *Biosensors*, 2012, **2**, 57–69.
- H. R. Holmes, E. Vlaisavljevich, E. L. Tan, K. L. Snyder, K. G. Ong and R. M. Rajachar, *J. Biomech.*, 2018, **71**, 199–207.



- 35 E. Vlaisavljevich, L. P. Janka, K. G. Ong and R. M. Rajachar, *IEEE Trans. Biomed. Eng.*, 2011, **58**, 698–704.
- 36 J. Xue, T. Wu, Y. Dai and Y. Xia, *Chem. Rev.*, 2019, **119**, 5298–5415.
- 37 Y. Li, J. Zhu, H. Cheng, G. Li, H. Cho, M. Jiang, Q. Gao and X. Zhang, *Adv. Mater. Technol.*, 2021, **6**, 2100410.
- 38 T. D. Brown, P. D. Dalton and D. W. Hutmacher, *Adv. Mater.*, 2011, **23**, 5651–5657.
- 39 J. C. Kade and P. D. Dalton, *Adv. Healthcare Mater.*, 2021, **10**, e2001232.
- 40 K. L. O'Neill and P. D. Dalton, *Small Methods*, 2023, **7**, 2201589.
- 41 B. L. Devlin, M. C. Allenby, J. Ren, E. Pickering, T. J. Klein, N. C. Paxton and M. A. Woodruff, *Adv. Funct. Mater.*, 2024, 2313092.
- 42 T. M. Robinson, D. W. Hutmacher and P. D. Dalton, *Adv. Funct. Mater.*, 2019, **29**, 1904664.
- 43 M. L. G. K. Włodarczyk-Biegun, M. Villiou, M. Koch, C. Muth, P. Wang, J. Ott and A. del Campo, *ACS Biomater. Sci. Eng.*, 2022, **8**, 3899–3911.
- 44 M. Castilho, A. van Mil, M. Maher, C. H. G. Metz, G. Hochleitner, J. Groll, P. A. Doevendans, K. Ito, J. P. G. Sluijter and J. Malda, *Adv. Funct. Mater.*, 2018, **28**, 1803153.
- 45 K. F. Eichholz, P. Pitacco, R. Burdis, F. Chariyev-Prinz, X. Barceló, B. Tornifoglio, R. Paetzold, O. Garcia and D. J. Kelly, *Adv. Healthcare Mater.*, 2023, **13**, 2302057.
- 46 *Metglas® 2826MB*, available online: <http://www.metglas.com> (accessed 25/01/2023).
- 47 S. Florczak, T. Lorson, T. Zheng, M. Mrlik, D. W. Hutmacher, M. J. Higgins, R. Luxenhofer and P. D. Dalton, *Polym. Int.*, 2019, **68**, 735–745.
- 48 S. Loewner, S. Heene, T. Baroth, H. Heymann, F. Cholewa, H. Blume and C. Blume, *Front. Bioeng. Biotechnol.*, 2022, **10**, 896719.
- 49 P. G. Saiz, A. Reizabal, S. Luposchainsky, J. L. Vilas-Vilela, S. Lanceros-Mendez and P. D. Dalton, *Adv. Mater. Technol.*, 2023, **8**, 2202063.
- 50 N. Abbasi, A. Abdal-hay, S. Hamlet, E. Graham and S. Ivanovski, *ACS Biomater. Sci. Eng.*, 2019, **5**, 3448–3461.
- 51 P. G. Saiz, J. M. Porro, A. Lasheras, R. F. de Luis, I. Quintana, M. I. Arriortua and A. C. Lopes, *J. Alloys Compd.*, 2021, **863**, 1–4.
- 52 M. von Witzleben, J. Hahn, R. F. Richter, B. de Freitas, E. Steyer, K. Schütz, C. Vater, A. Bernhardt, C. Elschner and M. Gelinsky, *Biomater. Adv.*, 2024, **156**, 213708.
- 53 N. C. Paxton, M. Lanaro, A. Bo, N. Crooks, M. T. Ross, N. Green, K. Tetsworth, M. C. Allenby, Y. Gu, C. S. Wong, S. K. Powell and M. A. Woodruff, *J. Mech. Behav. Biomed. Mater.*, 2020, **105**, 103695.
- 54 C. M. Brennan, K. F. Eichholz and D. A. Hoey, *Biomed. Mater.*, 2019, **14**, 065016.

